



# Evidence for $B^+ \rightarrow K^+ \nu \bar{\nu}$ decays

(Supplemental Material)

April 9, 2024

## I. INPUT VARIABLES FOR THE CLASSIFIERS

### A. ITA

In total, 36 variables are used as inputs to the classifiers in the ITA. Among these variables, 12 are used to train the first classifier:  $\Delta E_{\text{ROE}}$ , Modified Fox-Wolfram  $H_{m,2}^{\text{so}}$ , Modified Fox-Wolfram  $H_{m,4}^{\text{so}}$ , Harmonic Moment  $B_0$ ,  $p_{\text{ROE}}$ , Modified Fox-Wolfram  $R_2^{\text{so}}$ , Modified Fox-Wolfram  $R_0^{\text{so}}$ , Fox-Wolfram  $R_1$ ,  $\cos(\text{thrust}_B, \text{thrust}_{\text{ROE}})$ ,  $\theta(p_{\text{ROE}})$ ,  $\cos(\theta(\text{thrust}))$ , and Harmonic Moment  $B_2$ . Apart from Harmonic Moment  $B_2$ , the other 35 variables are used to train the second classifier.

Figures 1 to 6 show the distributions of the 36 variables at pre-selection level with 1% of data in the ITA.

- Fox-Wolfram  $R_1$ , first normalized Fox-Wolfram moment in the c.m. frame
- Fox-Wolfram  $R_2$ , second normalized Fox-Wolfram moment in the c.m. frame
- Fox-Wolfram  $R_3$ , third normalized Fox-Wolfram moment in the c.m. frame
- Sphericity, event sphericity in the c.m. frame
- Harmonic Moment  $B_0$ , zeroth-order harmonic moment with respect to the thrust axis in the c.m. frame
- Harmonic Moment  $B_2$ , second-order harmonic moment with respect to the thrust axis in the c.m. frame
- Modified Fox-Wolfram  $H_{c,2}^{\text{so}}$ , second-order modified Fox-Wolfram moment related to charged particles in the ROE calculated in the c.m. frame
- Modified Fox-Wolfram  $H_{n,2}^{\text{so}}$ , second-order modified Fox-Wolfram moment related to neutral particles calculated in the c.m. frame
- Modified Fox-Wolfram  $H_{m,2}^{\text{so}}$ , second-order modified Fox-Wolfram moment related to missing momentum calculated in the c.m. frame
- Modified Fox-Wolfram  $H_{m,4}^{\text{so}}$ , fourth-order modified Fox-Wolfram moment related to missing momentum calculated in the c.m. frame
- $d_r(K^+, \text{Tag Vertex})$ , radial distance between the POCA of the  $K^+$  candidate track and the tag vertex
- $d_z(K^+, \text{Tag Vertex})$ , longitudinal distance between the POCA of the  $K^+$  candidate track and the tag vertex
- $N_{\text{lepton}}$ , number of  $e^\pm$  and  $\mu^\pm$  candidates
- $N_\gamma$ , number of photon candidates
- $N_{\text{tracks}}$ , number of charged particle candidates
- $e^2$ , square of the total charge of tracks in the event
- $M_{\text{missing}}^2$ , square of the missing invariant mass
- $\theta(p_{\text{missing}})$ , polar angle of the missing three-momentum in the c.m. frame
- $\cos(\theta(\text{thrust}))$ , cosine of the polar angle of the thrust axis in the c.m. frame
- $\cos(\text{thrust}_K, \text{thrust}_{\text{ROE}})$ , cosine of the angle between the thrust axis of the  $K$  candidate and the thrust axis of the ROE computed in the c.m. frame
- $\cos(\text{thrust}_B, z)$ , cosine of the angle between the thrust axis of the signal  $B$  candidate and the  $z$  axis
- $\Delta E_{\text{ROE}}$ , difference between the ROE energy and the energy of one beam ( $\sqrt{s}/2$ ) both computed in the c.m. frame
- $\theta(p_{\text{ROE}})$ , polar angle of the ROE momentum
- $p_{\text{ROE}}$ , magnitude of the ROE momentum
- $d_r(K^+)$ , radial distance between the POCA of the  $K^+$  candidate track and the IP

- $\text{Var}(p_T^i | i \in \text{ROE})$ , variance of the transverse momentum of the ROE tracks
- Modified Fox-Wolfram  $R_0^{\text{oo}}$ , moment of the “oo” type (i.e. ROE-ROE), calculated in the c.m. frame
- Modified Fox-Wolfram  $R_2^{\text{oo}}$ , moment of the “oo” type (i.e. ROE-ROE), calculated in the c.m. frame
- $d_x(\text{Tag Vertex})$ ,  $x$  component of the vector from the IP to the tag vertex
- $d_z(\text{Tag Vertex})$ ,  $z$  component of the vector from the IP to the tag vertex
- $p\text{-value}(\text{ROE})$ ,  $p$ -value of the ROE tag vertex fit
- $M(K^+X^-)$ , invariant mass for the candidate  $K^+$  plus a charged particle from the ROE
- $\text{Median}(p\text{-value}(D^0))$ , median  $p$ -value of the vertex fits of the  $D^0$  candidates
- $p\text{-value}(D^0)$ ,  $p$ -value of the best  $D^0$  candidate vertex fit
- $p\text{-value}(D^+)$ ,  $p$ -value of the best  $D^+$  candidate vertex fit
- $d_r(D^+)$ , radial distance between the best  $D^+$  candidate vertex and the IP

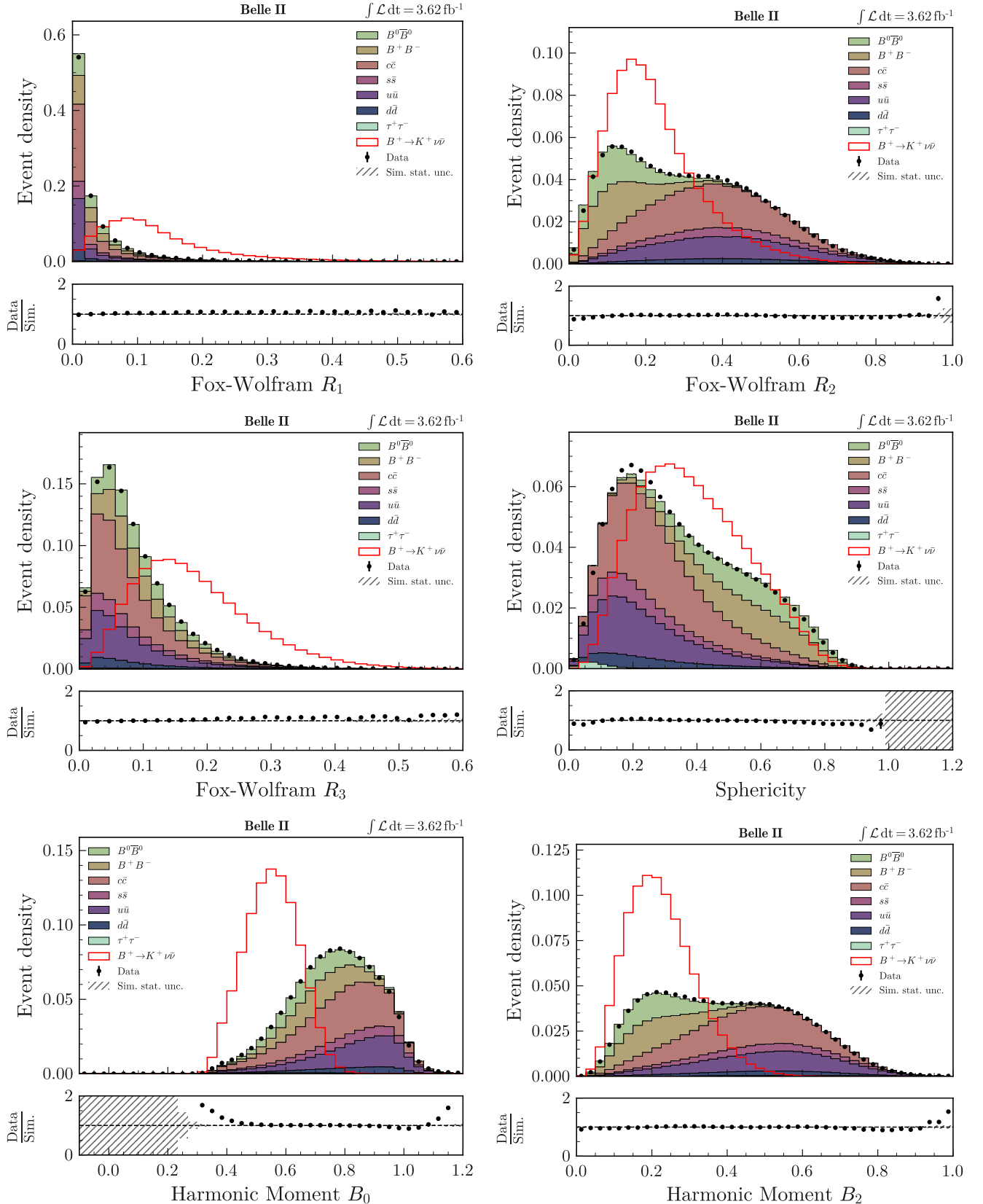


FIG. 1. Simulated signal and background and data event density of Fox-Wolfram  $R_1$ , Fox-Wolfram  $R_2$ , Fox-Wolfram  $R_3$ , Sphericity, Harmonic Moment  $B_0$  and Harmonic Moment  $B_2$ , in the ITA.

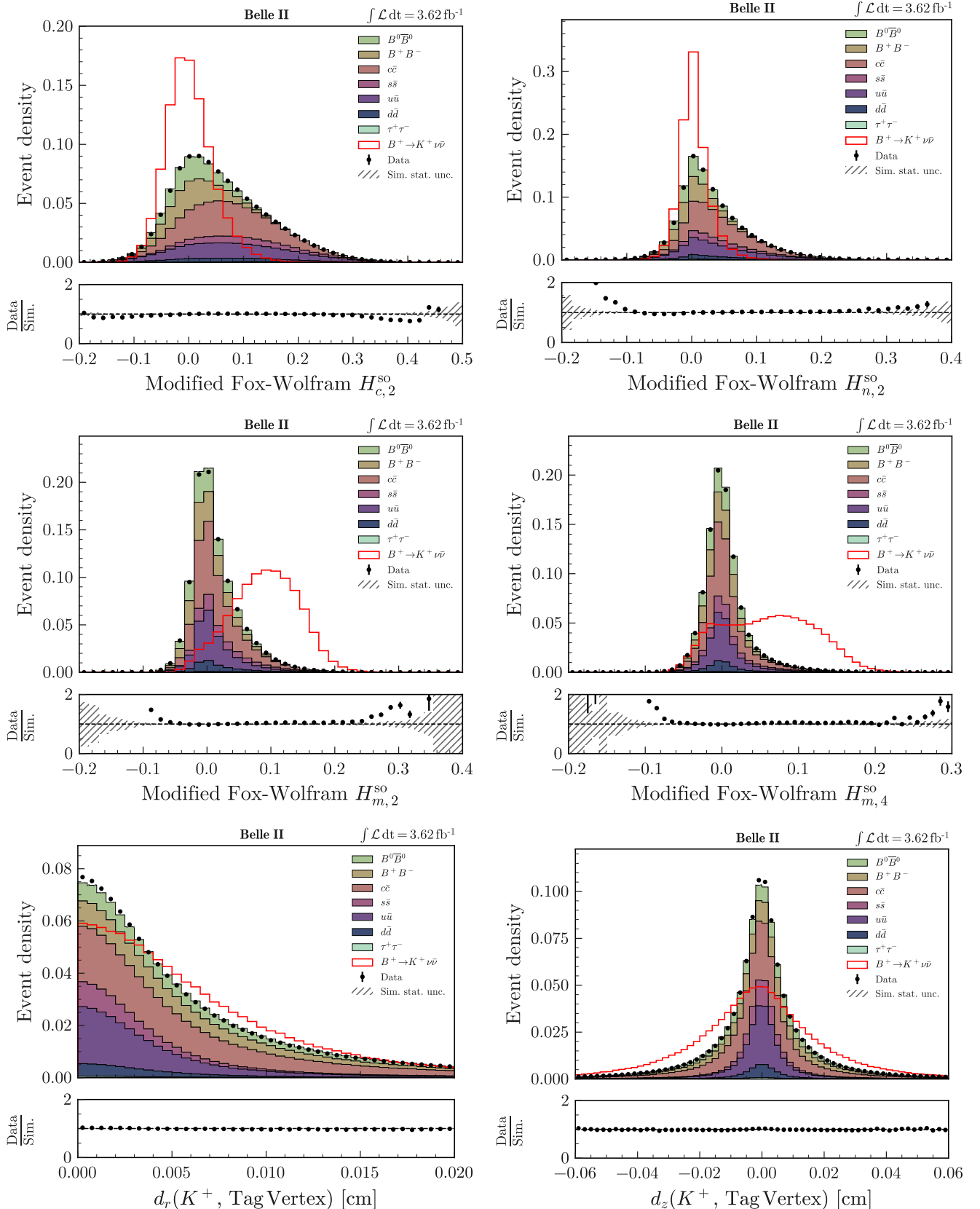


FIG. 2. Simulated signal and background and data event density of Modified Fox-Wolfram  $H_{n,2}^{\text{so}}$ , Modified Fox-Wolfram  $H_{m,2}^{\text{so}}$ , Modified Fox-Wolfram  $H_{m,4}^{\text{so}}$ ,  $d_r(K^+, \text{Tag Vertex})$  and  $d_z(K^+, \text{Tag Vertex})$  in the ITA.

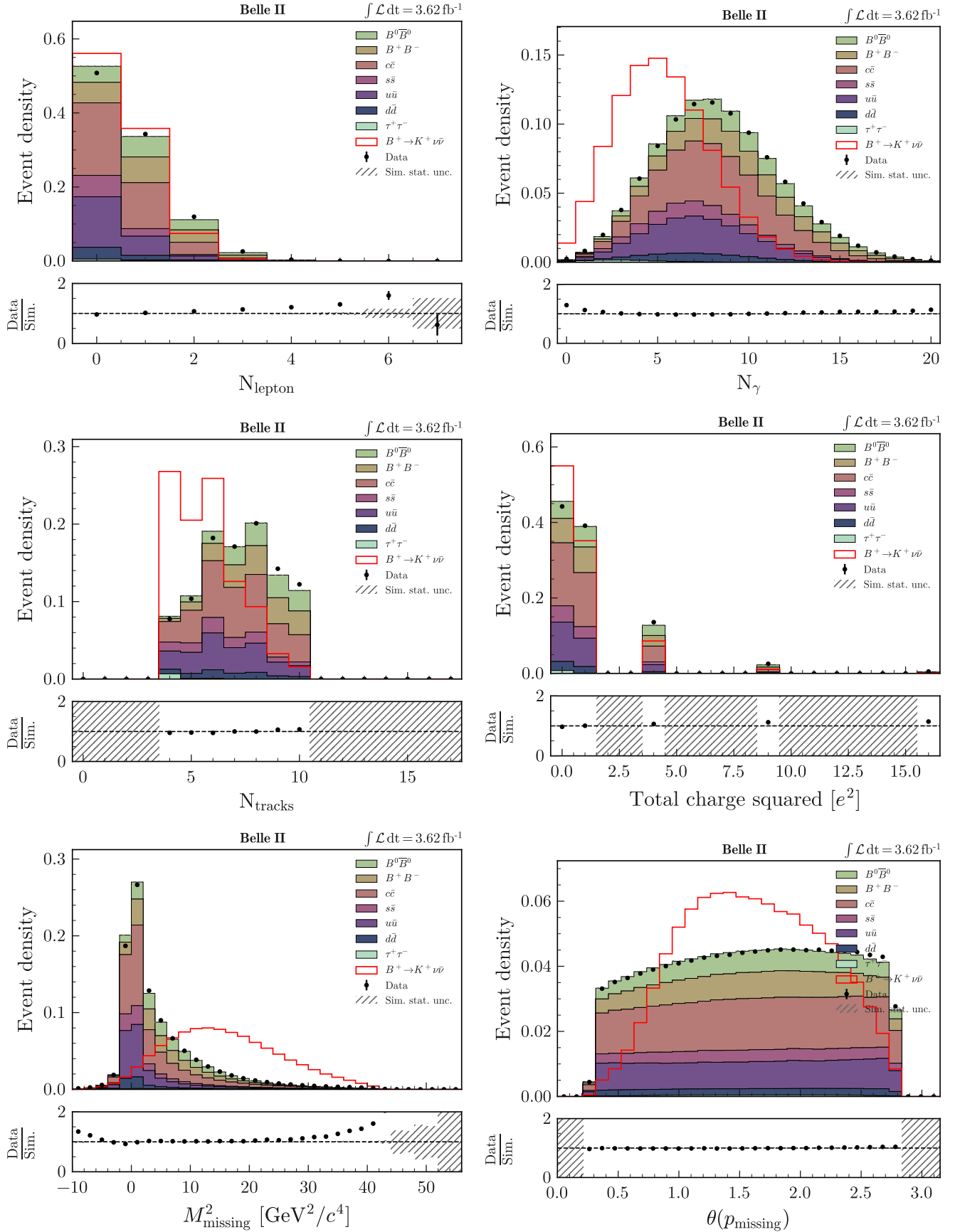


FIG. 3. Simulated signal and background and data event density of  $N_{\text{lepton}}$ ,  $N_{\gamma}$ ,  $N_{\text{tracks}}$ ,  $e^2$ ,  $M_{\text{missing}}^2$  and  $\theta(p_{\text{missing}})$  in the ITA.

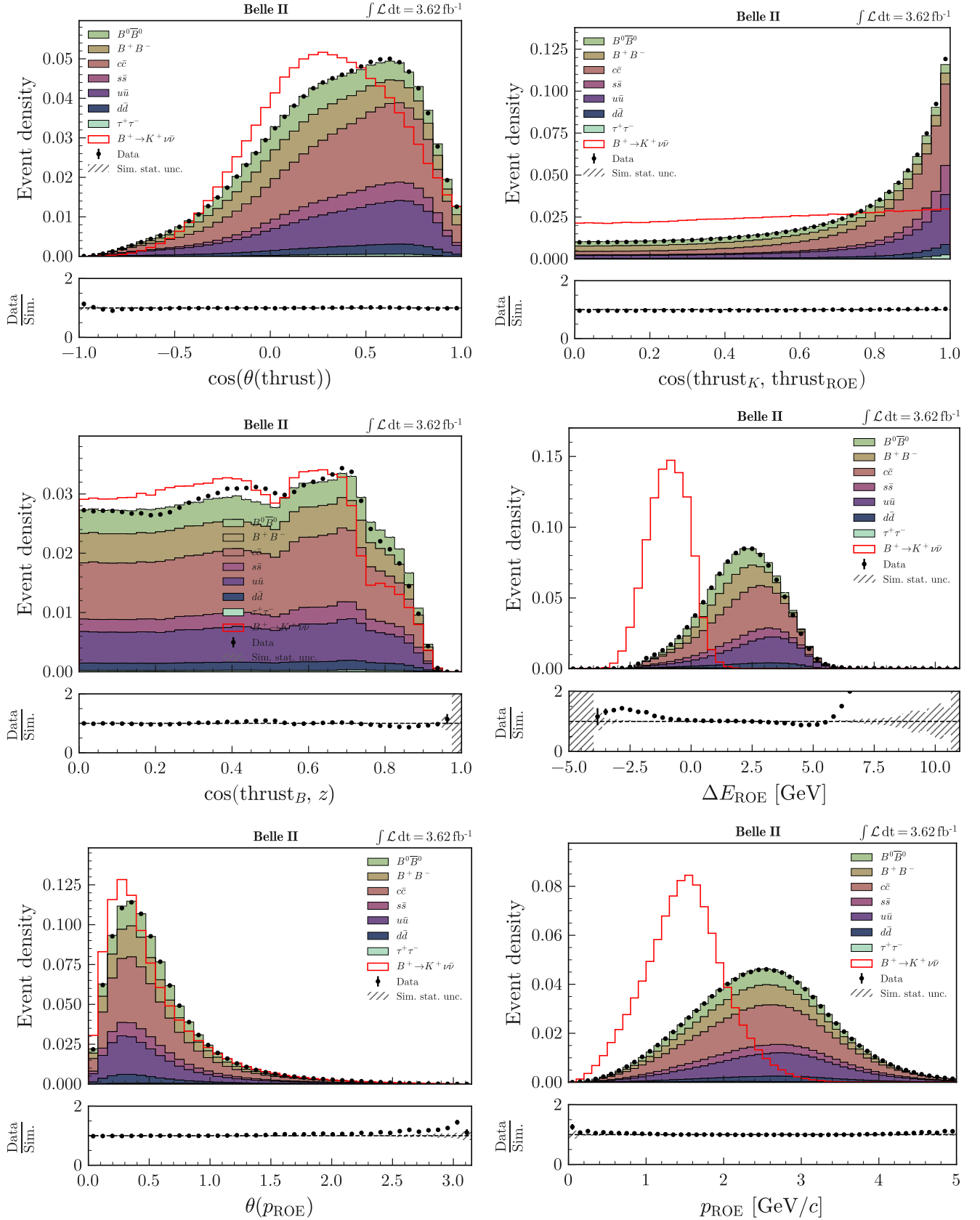


FIG. 4. Simulated signal and background and data event density of  $\cos(\theta(\text{thrust}))$ ,  $\cos(\text{thrust}_K, \text{thrust}_{\text{ROE}})$ ,  $\cos(\text{thrust}_B, z)$ ,  $\Delta E_{\text{ROE}}$ ,  $\theta(p_{\text{ROE}})$  and  $p_{\text{ROE}}$  in the ITA.

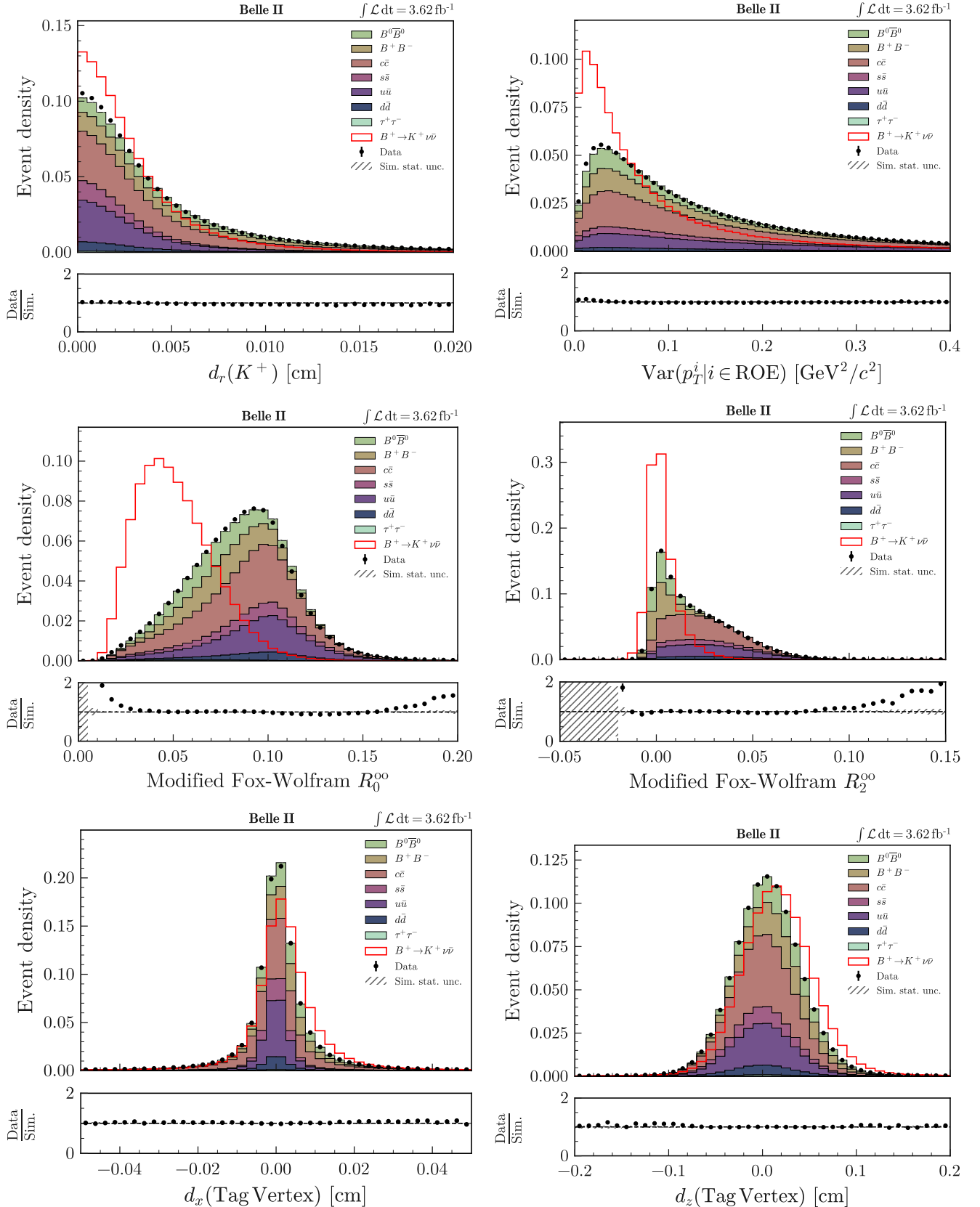


FIG. 5. Simulated signal and background and data event density of  $d_r(K^+)$ ,  $\text{Var}(p_T^i | i \in \text{ROE})$ , Modified Fox-Wolfram  $R_0^{oo}$ , Modified Fox-Wolfram  $R_2^{oo}$ ,  $d_x(\text{Tag Vertex})$  and  $d_z(\text{Tag Vertex})$  in the ITA.

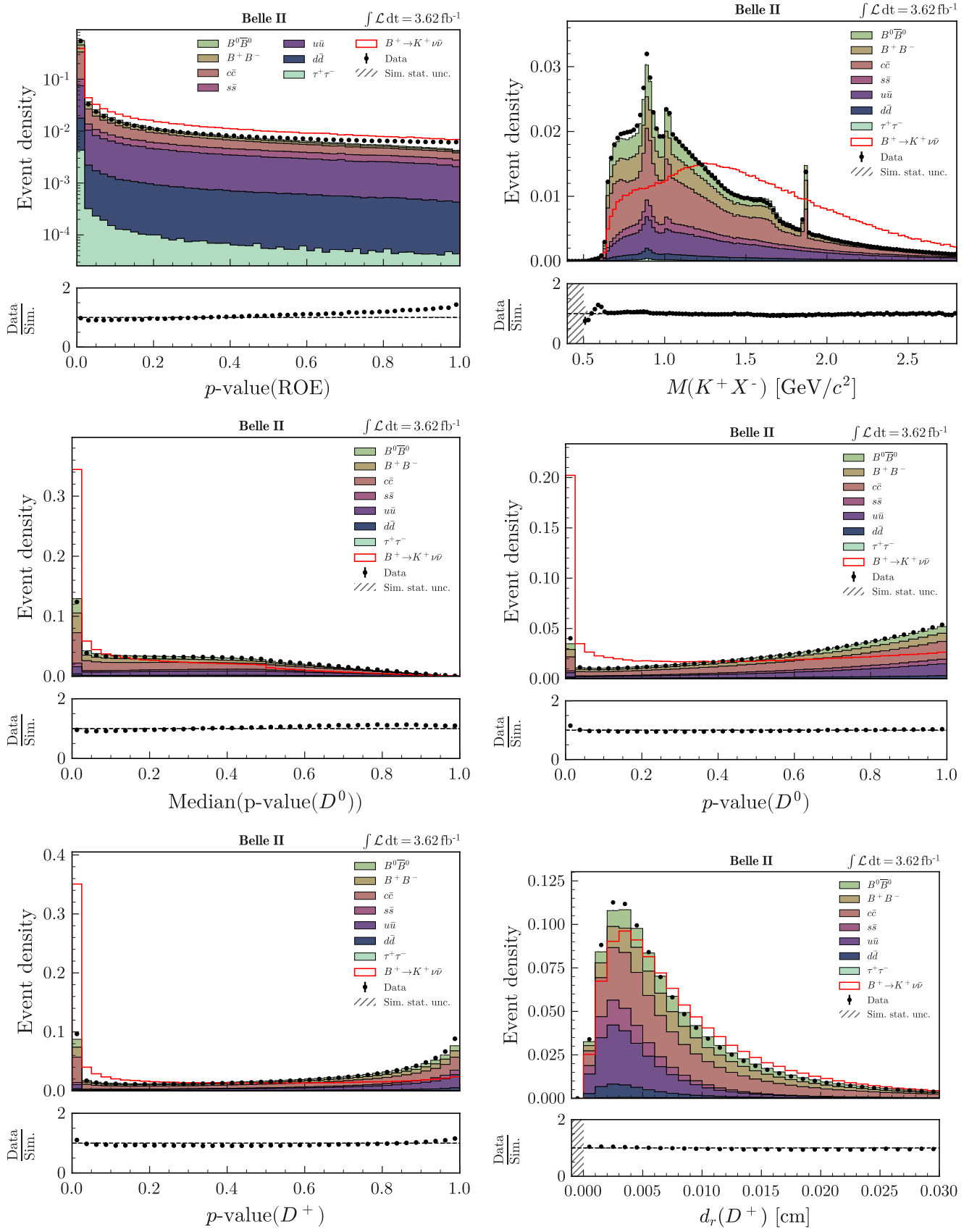


FIG. 6. Simulated signal and background and data event density of  $p\text{-value(ROE)}$ ,  $M(K^+X^-)$ ,  $\text{Median}(p\text{-value}(D^0))$ ,  $p\text{-value}(D^0)$ ,  $p\text{-value}(D^+)$  and  $d_r(D^+)$  in the ITA.

## B. HTA

Figures 7 and 8 show the distributions, at pre-selection level, of the 12 variables used to train the selection BDTh in the HTA.

- $n_{\text{tracks extra}}$ , number of extra tracks surviving track quality selection
- $M_{\text{recoil}}$ , recoil mass
- $H_{m,2}^{\text{so}}$ , second-order modified Fox-Wolfram moment related to missing momentum calculated in the c.m. frame
- $H_{c,2}^{\text{so}}$ , second-order modified Fox-Wolfram moment related to charged particles in the  $B_{\text{tag}}$  and the extra tracks, calculated in the c.m. frame
- $R_0^{\text{oo}}$ , zeroth-order modified Fox-Wolfram moment within the system formed by the objects comprising the  $B_{\text{tag}}$ , the extra tracks, and the extra photons (“oo”) calculated in the c.m. frame
- $\cos(\text{thrust}_K, \text{thrust}_{\text{other}})$ , cosine of the angle between the thrust axis of the signal kaon candidate and the thrust axis of all other reconstructed objects (those comprising the  $B_{\text{tag}}$ , the extra tracks, and the extra photons) computed in the c.m. frame
- $\phi^*(K^+, p_{\text{miss}})$ , azimuthal angle between the signal kaon and the missing momentum direction in the c.m. frame
- $E_{\text{miss}}^* + cp_{\text{miss}}^*$ , sum of missing momentum and energy in the c.m. frame
- $E_{\text{extra}}$ , sum of extra-photon energy
- $B_{\text{tag}}$  signal probability, probability of the reconstructed  $B_{\text{tag}}$  correctly describing the true process returned by the FEI
- $p\text{-value}(D^0)$ ,  $p$ -value of the best  $D^0$  candidate vertex fit
- $p\text{-value}(D^+)$ ,  $p$ -value of the best  $D^+$  candidate vertex fit

## II. CORRECTIONS TO SIMULATED DATA

### A. Illustration of the validation of the hadronic energy correction in the ITA

Figure 9 shows the distribution of the number of photon candidates with hadronic energy scaled by  $-10\%$  (left), with hadronic energy scaled by  $+10\%$  (right) and with the nominal configuration (middle). Selections  $\text{BDT}_1 > 0.9$  and  $\eta(\text{BDT}_2) > 0.75$  are applied to both the simulated continuum background and the off-resonance data. In addition, the simulated continuum has been reweighted based on  $\text{BDT}_c$  output, as described in Section IX.A.

Figure 10 shows the distributions of the number of photon candidates and  $\Delta E_{\text{ROE}}(\text{neutral})$ , computed using only photon candidates associated with the ROE, within the signal region (upper) and the high-sensitivity region (lower).

### B. Signal selection efficiency validation in HTA

Figure 11 shows the BDTh output after candidate selection in the embedding sample.

### C. Validation of particle-identification correction

Figure 12 shows the distribution of  $q_{\text{rec}}^2$  obtained in  $B^+ \rightarrow \bar{D}^0(\rightarrow K^+\pi^-)h^+$  ( $h = K, \pi$ ) data and simulation. The kaon from  $\bar{D}^0$  is required to satisfy a kaon-enriching selection. The requirements  $\text{BDT}_1 > 0.9$  and  $\eta(\text{BDT}_2) > 0.92$  are also applied. The particle-identification corrections are applied on simulated data.

### D. Validation of $K_L^0$ efficiency

Figure 13 shows the distribution of energy deposits in the ECL matched to the  $K_L^0$  particle trajectory obtained in  $e^+e^- \rightarrow \phi(\rightarrow K_L^0 K_S^0)\gamma_{\text{ISR}}$  data and simulation. The events are selected by demanding a photon candidate with an energy  $E_\gamma > 4.7$  GeV in the c.m. frame, a well-reconstructed  $K_S^0$  candidate, and no extra tracks.

## III. BACKGROUND STUDIES

### A. Background composition in the ITA

Figure 14 shows the relative contributions of the various background components for charged  $B$  (left) and neutral  $B$  (right) decays in the signal region.

Figure 15 shows the distributions of  $q_{\text{rec}}^2$  in data and simulation with various charged and neutral  $B$  decay backgrounds shown by category.

### B. Illustration of improvement in the ITA with $\text{BDT}_c$ -based reweighting

Figure 16 shows the distribution of Fox-Wolfram Moment  $R_2$  without (left) and with (right) reweighting of the simulated continuum background based on  $\text{BDT}_c$  output, as described in Section IX.A. Selections  $\text{BDT}_1 > 0.9$  and  $\eta(\text{BDT}_2) > 0.75$  are applied to both the simulated continuum background and the off-resonance data.

### C. Additional figures for modeling of $D$ -meson decays involving a $K_L^0$ meson

Figure 17 shows the distribution of  $q_{\text{rec}}^2$  in simulation for  $B$ -meson decays with subsequent  $D^+ \rightarrow K_L^0 X$  and  $D^0 \rightarrow K_L^0 X$  decays in the pion-enriched control sample. As the distributions have a similar shape, these background components are treated together rather than separately.

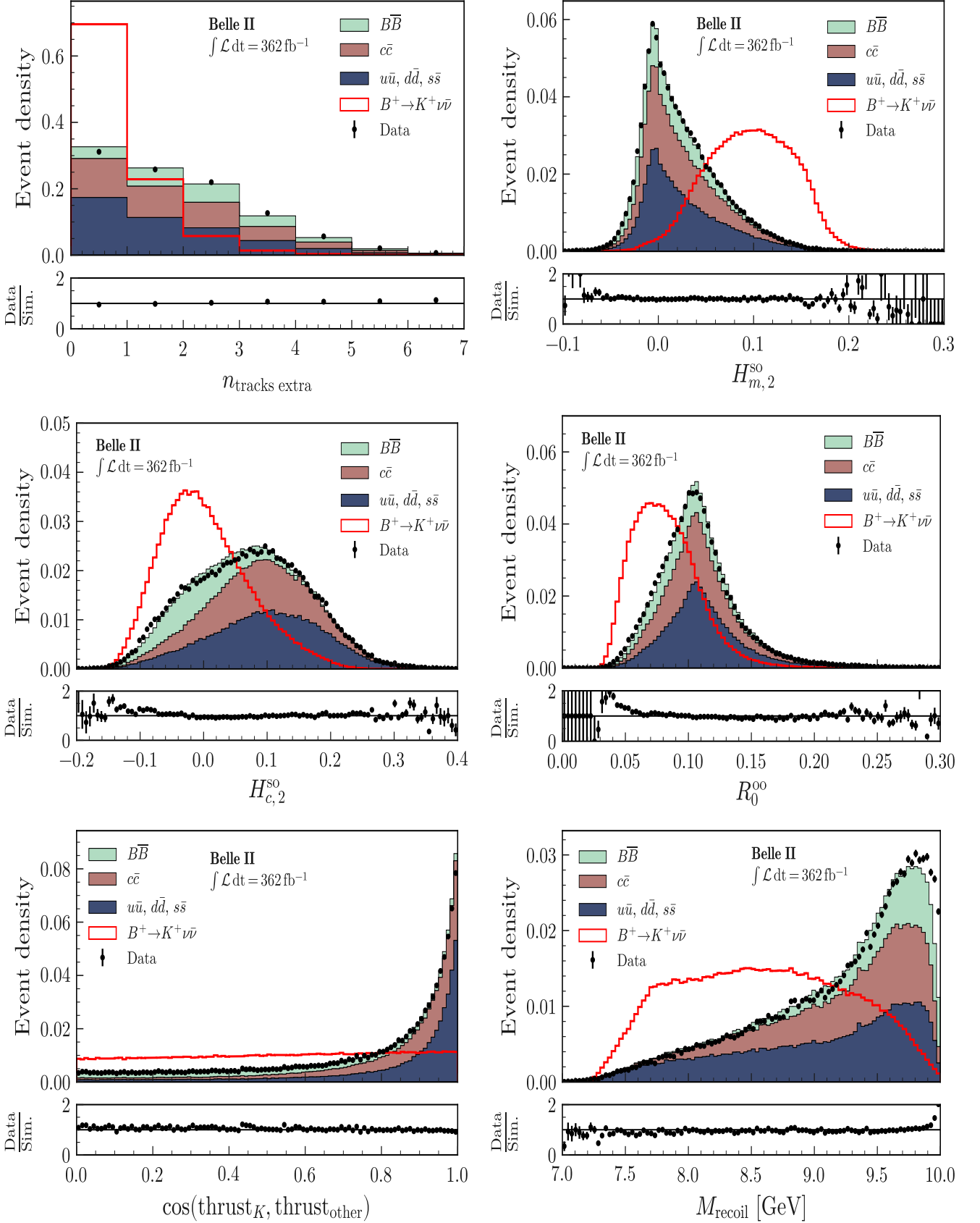


FIG. 7. Simulated signal and background and data event density of  $n_{\text{tracks extra}}$ ;  $M_{\text{recoil}}$ ; the modified Fox-Wolfram moments  $H_{m,2}^{\text{so}}$ ,  $H_{c,2}^{\text{so}}$ ,  $R_0^{\text{oo}}$ ; and  $\cos(\text{thrust}_K, \text{thrust}_{\text{other}})$ ; in the HTA.

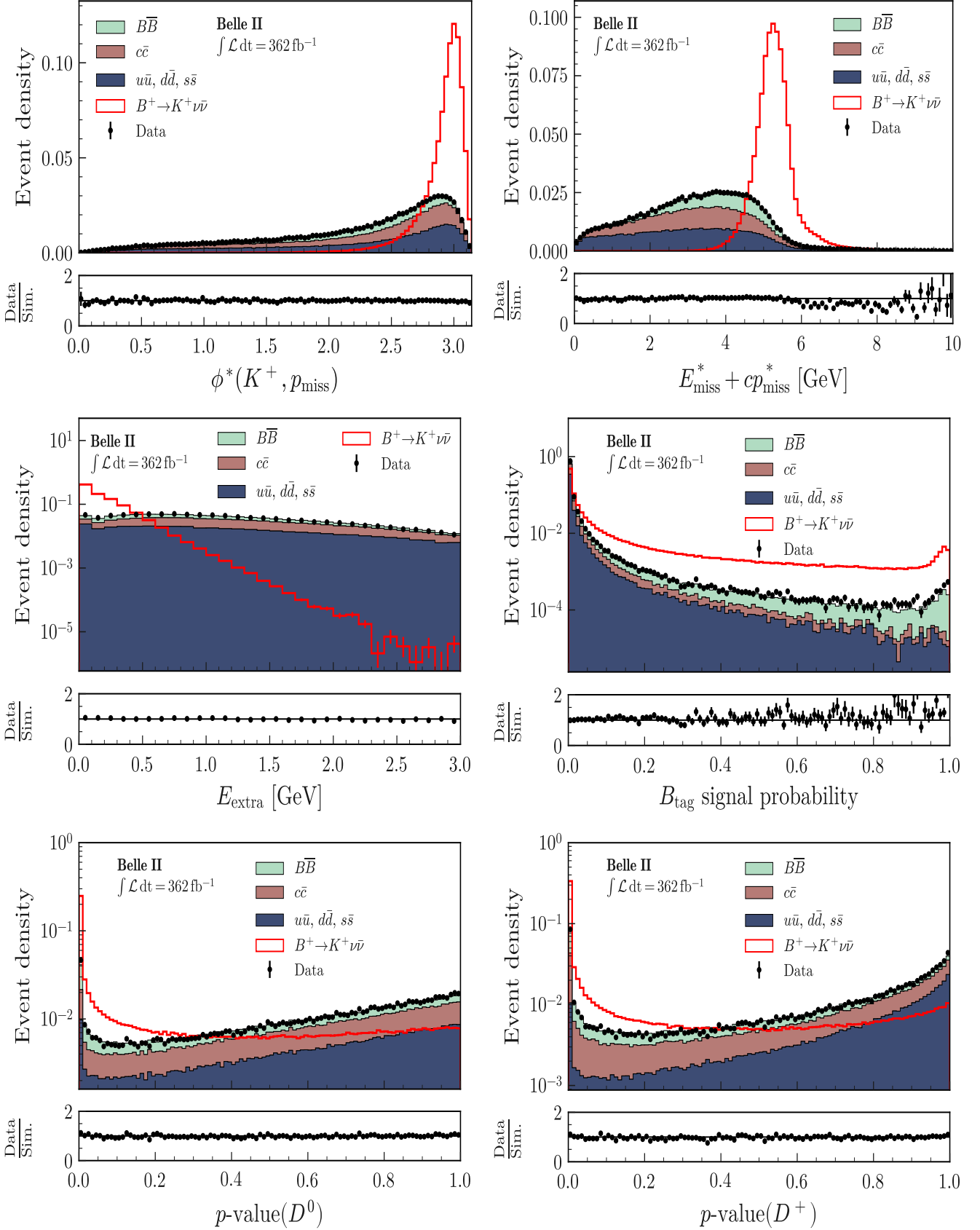


FIG. 8. Simulated signal and background and data event density of  $\phi^*(K^+, p_{\text{miss}})$ ,  $E_{\text{miss}}^* + cp_{\text{miss}}^*$ ,  $E_{\text{extra}}$ ,  $B_{\text{tag}}$  signal probability,  $p\text{-value}(D^0)$  and  $p\text{-value}(D^+)$ , in the HTA.

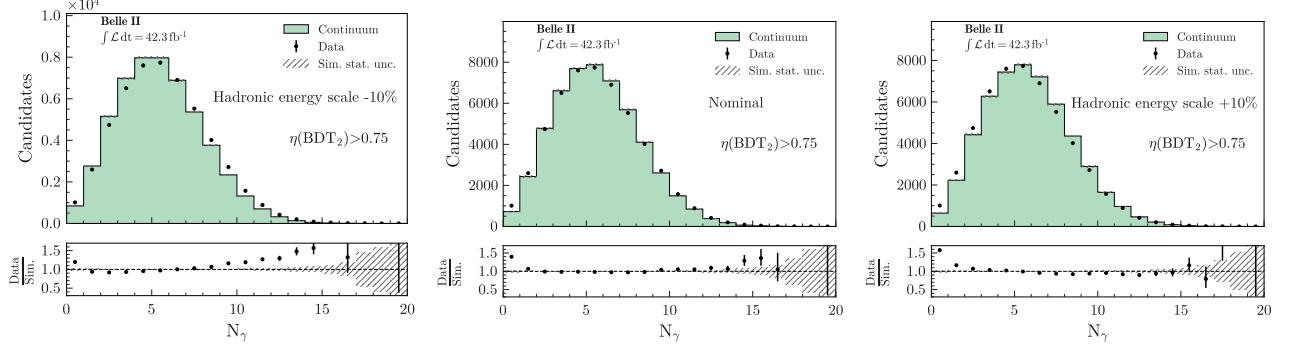


FIG. 9. The number of photon candidates with hadronic energy scaled by  $-10\%$  (left), at its nominal value (center), and scaled by  $+10\%$  (right) for simulated continuum background and off-resonance data. The simulation has been reweighted as described in the text.

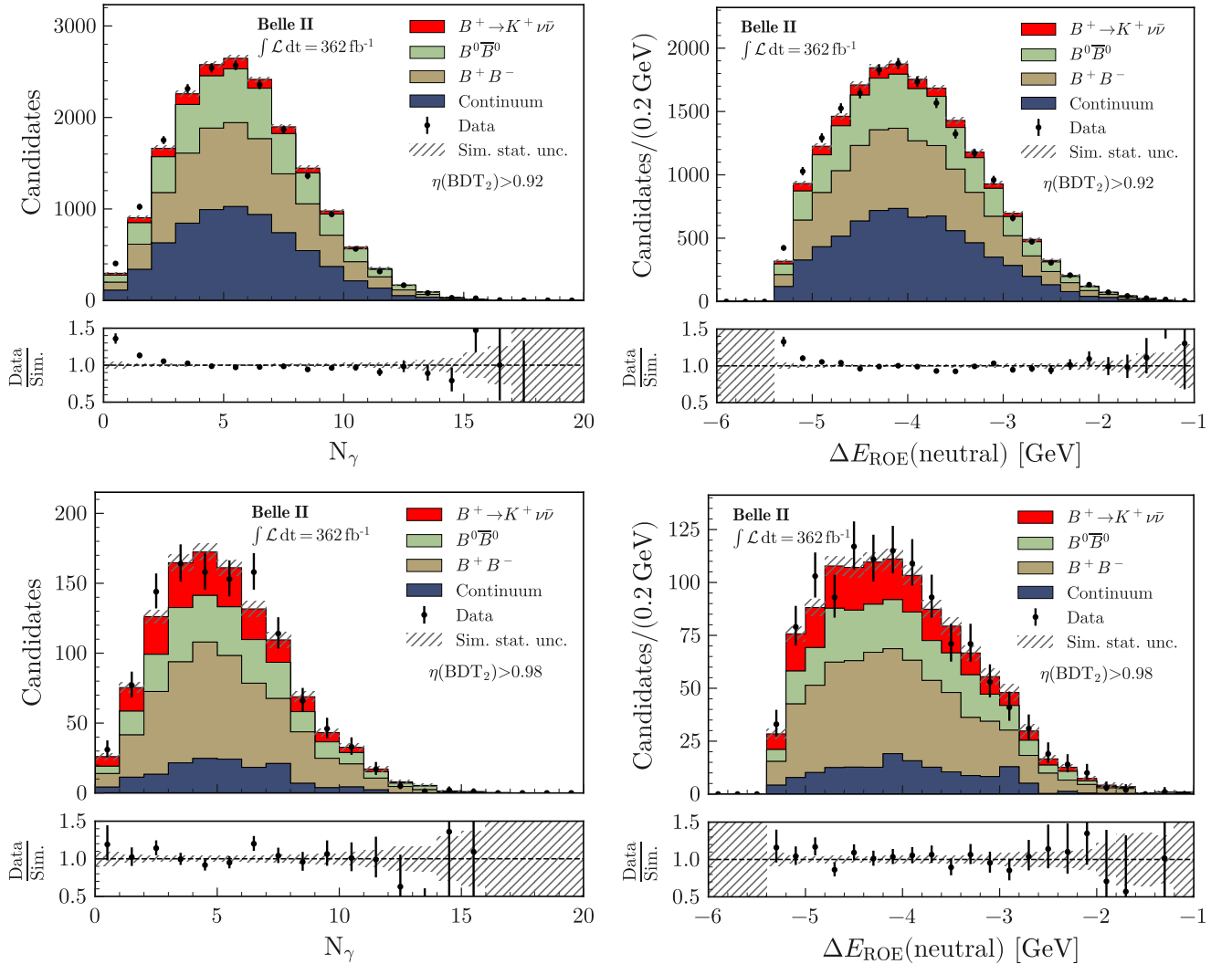


FIG. 10. Distributions of  $N_\gamma$  and  $\Delta E_{\text{ROE}}(\text{neutral})$  in data (points with error bars) and simulation (filled histograms) shown individually for the  $B^+ \rightarrow K^+ \nu \bar{\nu}$  signal, neutral and charged  $B$ -meson decays, and the sum of the five continuum categories in the ITA. Events in the full signal region, with  $\eta(\text{BDT}_2) > 0.92$  (upper plots) and with  $\eta(\text{BDT}_2) > 0.98$  (lower plots), are shown. Simulated samples are normalized according to the fit yields in the ITA. The data to simulation ratio are shown in the bottom panels.

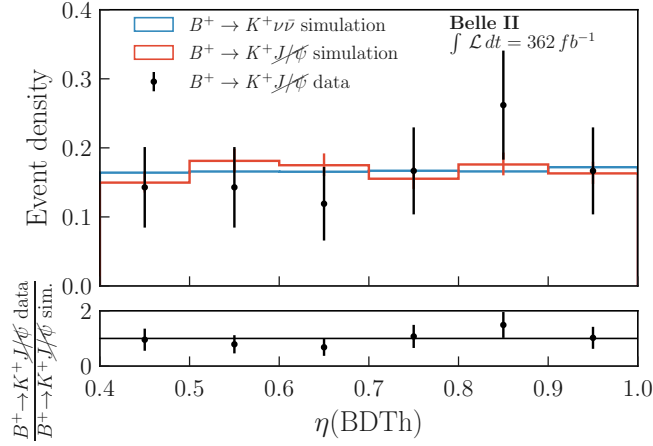


FIG. 11. Comparison of classifier output between the simulated signal sample, the signal embedding data and the signal embedding simulated sample in the HTA.

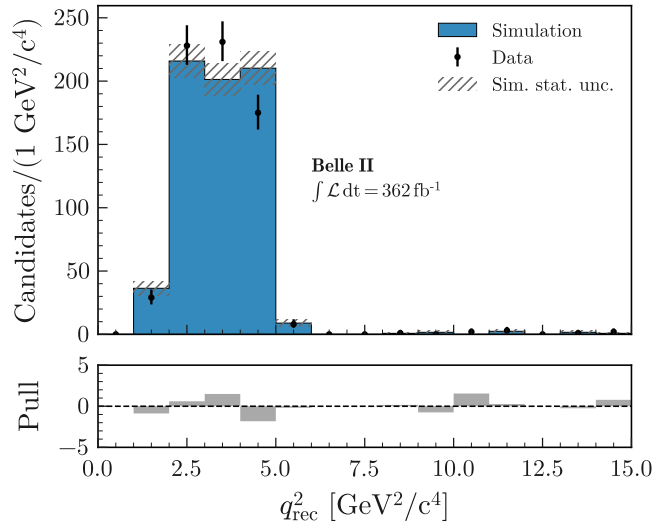


FIG. 12. Distribution of  $q_{\text{rec}}^2$  obtained for the  $B^+ \rightarrow \bar{D}^0(\rightarrow K^+ \pi^-)h^+$  candidates in data and  $B^+ B^-$  simulation. The samples are restricted to  $\bar{D}^0$ -daughter  $K^+$  candidates satisfying a kaon-enriching selection, and the selections  $\text{BDT}_1 > 0.9$  and  $\eta(\text{BDT}_2) > 0.92$ . The particle-identification correction weights are applied to the simulated sample.

#### IV. SIGNAL EXTRACTION

Figure 18 shows the expected background and signal in the signal search region, divided into 4 bins of  $\eta(\text{BDT}_2)$  and 3 bins of  $q_{\text{rec}}^2$  in the ITA.

#### V. UPPER LIMIT IN THE HTA

The expected and observed upper limits on the branching fraction are determined for the HTA using the  $\text{CL}_s$  method [1], a modified frequentist approach which is based on a profile likelihood ratio [2]. The expected 90% confidence level upper limit on the  $B^+ \rightarrow K^+ \nu \bar{\nu}$  branching fraction of  $1.8 \times 10^{-5}$  is derived assuming the background-only hypothesis. The observed upper limit is set at  $2.8 \times 10^{-5}$  at the 90% confidence level.

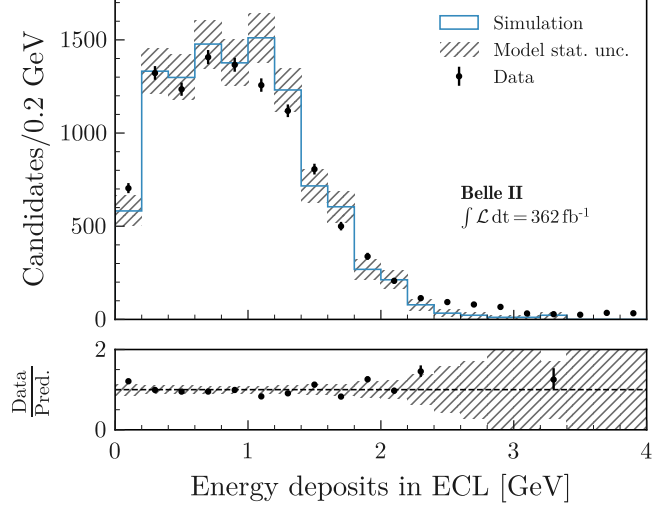


FIG. 13. Distribution of energy deposits in the ECL associated with the  $K_L^0$  particle obtained for the  $e^+e^- \rightarrow \phi(\rightarrow K_L^0 K_S^0)\gamma_{\text{ISR}}$  candidates in data and simulation. The events are selected by demanding a photon candidate with energy  $E_\gamma > 4.7$  GeV in the c.m. frame, a well-reconstructed  $K_S^0$  candidate, and no extra tracks.

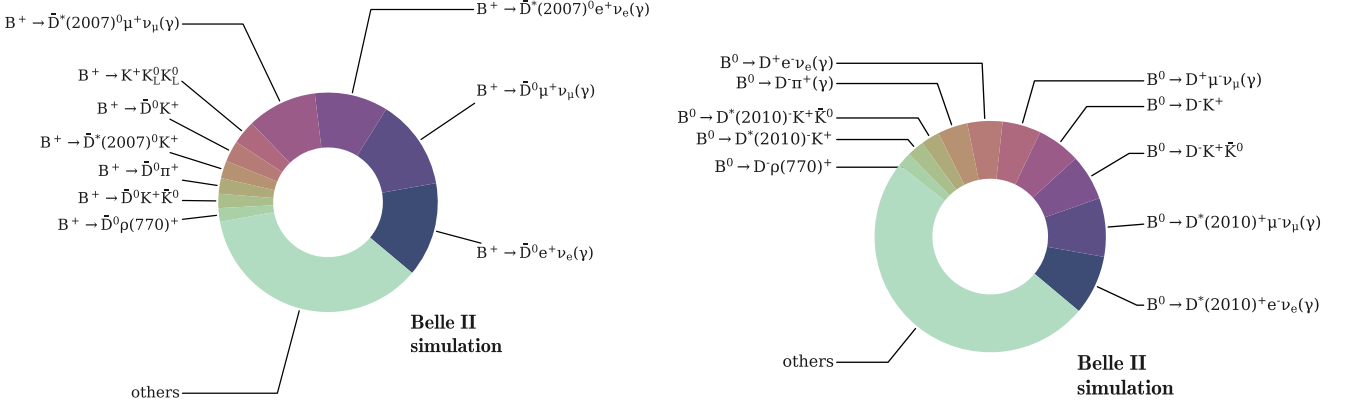


FIG. 14. Background components for charged  $B$  (left) and neutral  $B$  (right) decays in the signal region, in the ITA.

## VI. CROSS CHECK MEASUREMENT OF $B^+ \rightarrow \pi^+ K^0$

The inclusive tagging method is validated by performing a measurement of the branching fraction of the  $B^+ \rightarrow \pi^+ K^0$  decay, as described in Section XIII of the paper. The distribution of  $q_{\text{rec}}^2$  in the high sensitivity region with the background and signal components normalized using the fit result is shown in Fig. 19.

## VII. SIGNAL EFFICIENCY VALIDATION USING EMBEDDING

Figure 20 shows BDT<sub>1</sub> and BDT<sub>2</sub> outputs for the embedded samples. Compared to the figure shown in the main text, the distributions are presented using logarithmic scale for the  $y$ -axis.

- 
- [1] A. L. Read, Presentation of search results: the CLs technique, *J. Phys. G* **28**, 2693 (2002).
  - [2] G. Cowan, K. Cranmer, E. Gross, and O. Vitells, Asymptotic formulae for likelihood-based tests of new physics, *Eur. Phys. J. C* **71**, 1554 (2011), [73, 2501(E) (2013)].

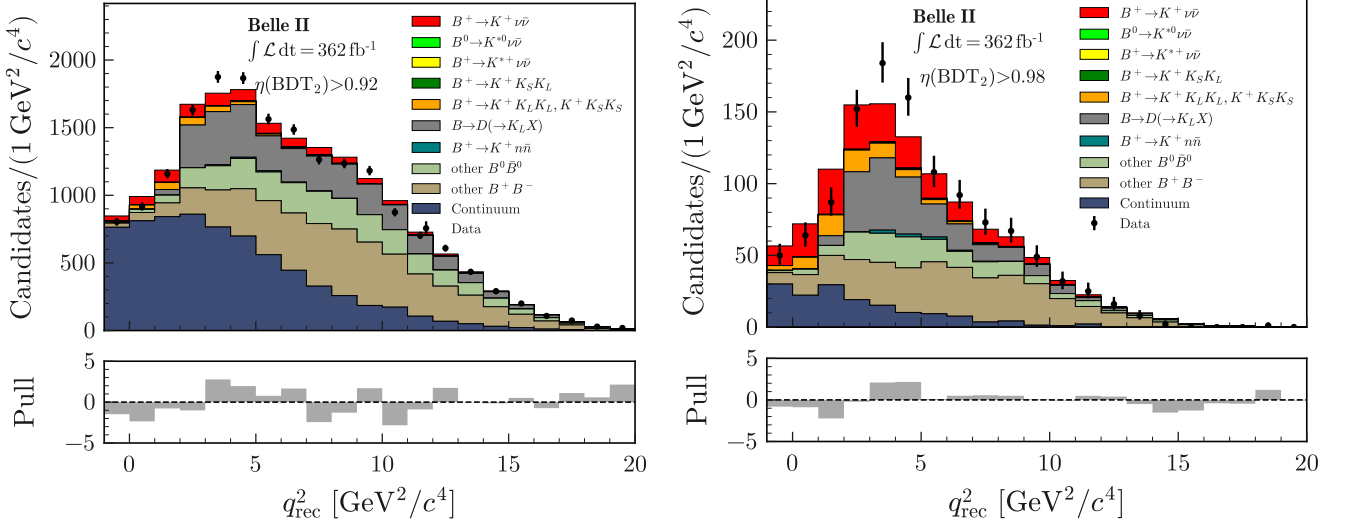


FIG. 15. Distributions of  $q_{\text{rec}}^2$  in data (points with error bars) and simulation (filled histograms) shown individually for the  $B^+ \rightarrow K^+ \nu \bar{\nu}$  signal, and for various categories of neutral and charged  $B$  decays in the ITA. The “other  $B^0 \bar{B}^0$ ” and “other  $B^+ B^-$ ” categories represent the  $B\bar{B}$  events that remain after subtracting the backgrounds shown in the legend. Events in the full signal region, with  $\eta(\text{BDT}_2) > 0.92$  (left), and high sensitivity region, with  $\eta(\text{BDT}_2) > 0.98$  (right), are shown. Simulated samples are normalized according to the fit yields in the ITA. The pull distributions are shown in the bottom panels.

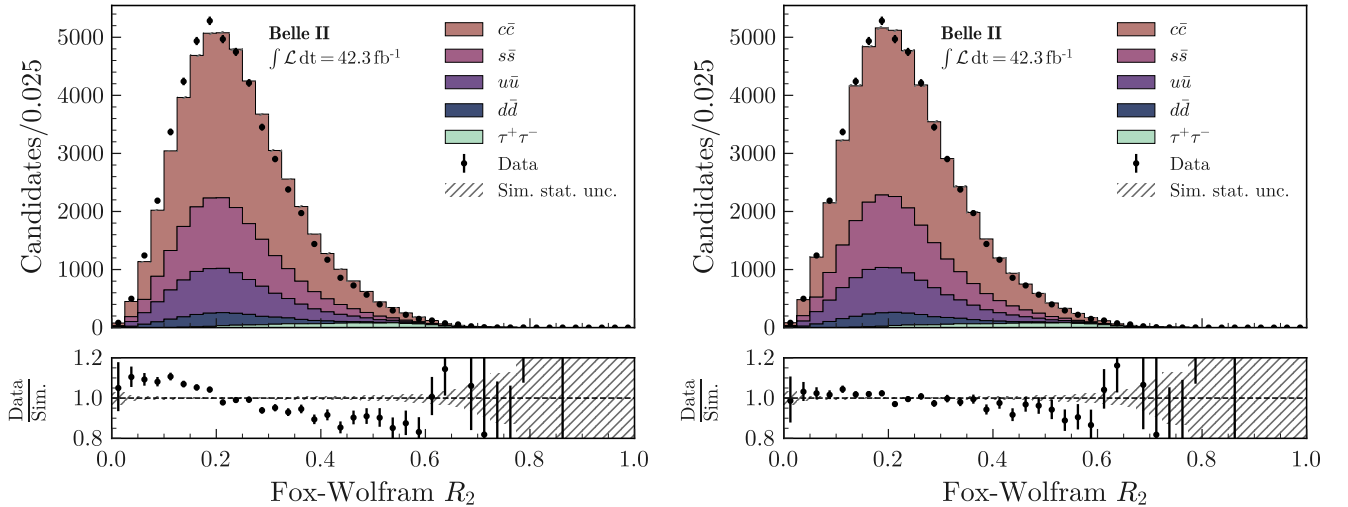


FIG. 16. Fox-Wolfram  $R_2$  without (left) and with (right) reweighting based on  $\text{BDT}_c$  output, as described in the text, in the ITA.

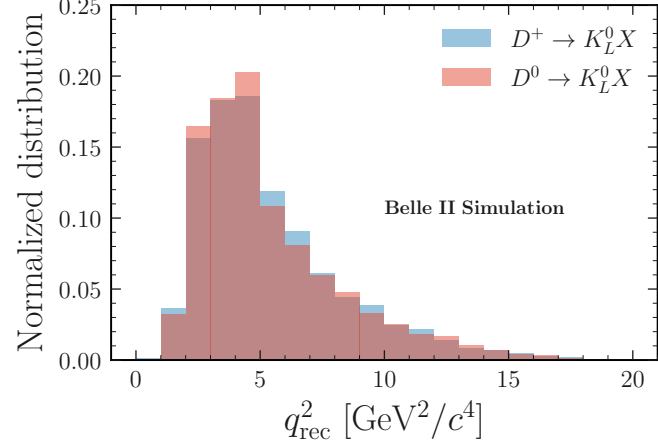


FIG. 17. Distribution of  $q_{\text{rec}}^2$  in simulation for  $B$ -meson decays with subsequent  $D^+ \rightarrow K_L^0 X$  and  $D^0 \rightarrow K_L^0 X$  decays in the pion-enriched control sample.

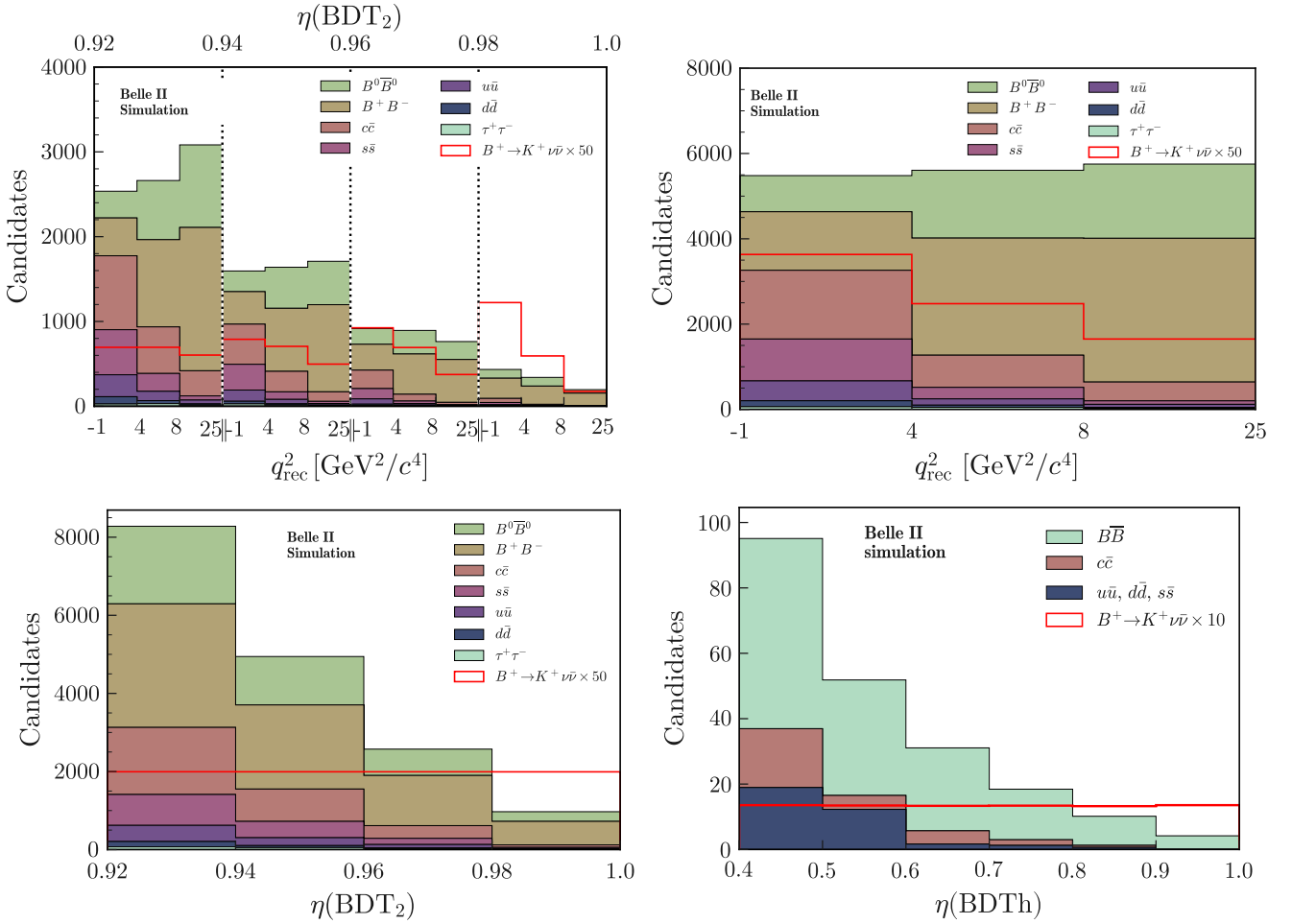


FIG. 18. Expected background and signal in the signal region for the ITA (top left), in projections of the signal region onto  $q_{\text{rec}}^2$  (top right) and  $\eta(\text{BDT}_2)$  (bottom left), and in the signal region for the HTA (bottom right).

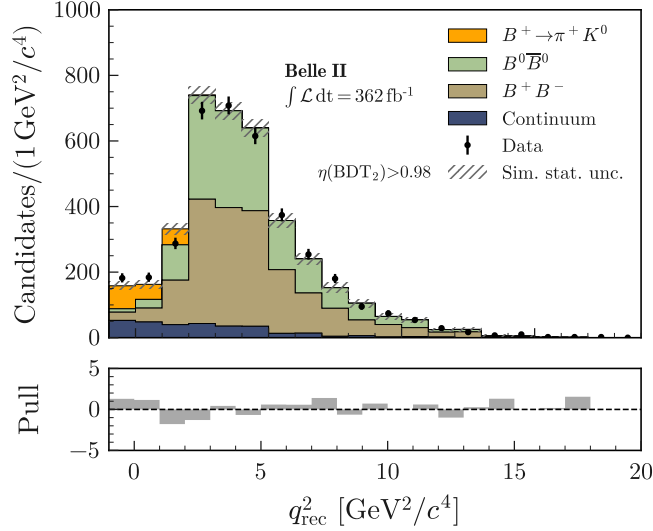


FIG. 19. Distribution of  $q_{\text{rec}}^2$  for ITA events in the pion-enriched sample and populating the  $\eta(\text{BDT}_2) > 0.98$  bins. The yields of simulated background and signal components are normalized based on the fit results to determine the branching fraction of the  $B^+ \rightarrow \pi^+ K^0$  decay. The pull distribution is shown in the bottom panel.

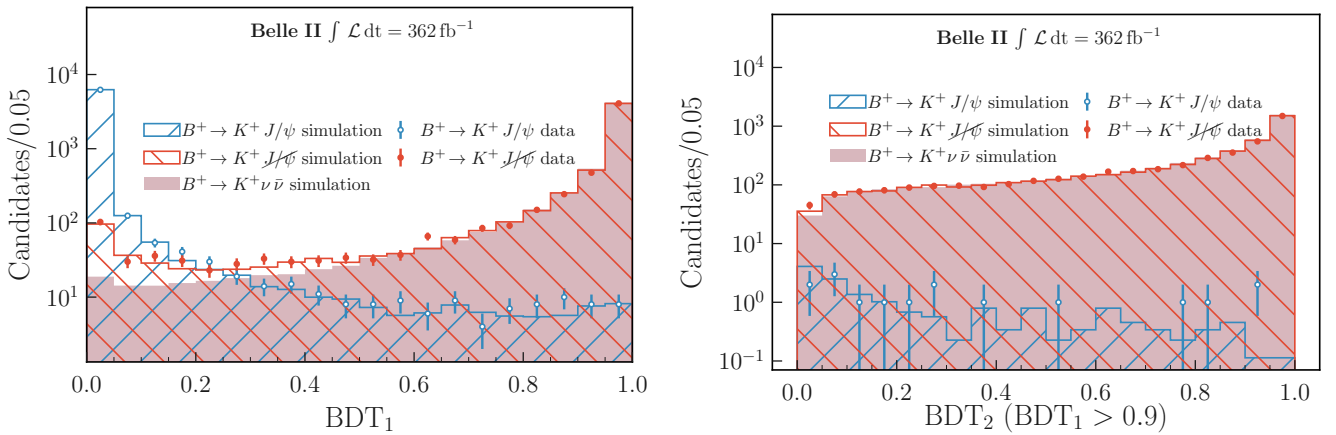


FIG. 20. Distributions of the classifier output BDT<sub>1</sub> (left) and BDT<sub>2</sub> (right). The distributions are shown before ( $B^+ \rightarrow K^+ J/\psi$ ) and after ( $B^+ \rightarrow K^+ J/\psi$ ) the muon removal and replacement of the kaon momentum of selected  $B^+ \rightarrow K^+ J/\psi$  events in simulation and data. As a reference, the classifier outputs directly obtained from simulated  $B^+ \rightarrow K^+ \nu \bar{\nu}$  signal events are overlaid. The simulation histograms are scaled to the total number of  $B^+ \rightarrow K^+ J/\psi$  events selected in the data.